Thermal conductivity in self-assembled CoFe 2 O 4 /BiFeO 3 vertical nanocomposite films

As Published: 10.1063/1.5049176

Publisher: AIP Publishing

Persistent URL: https://hdl.handle.net/1721.1/134914

Version: Final published version: final published article, as it appeared in a journal, conference proceedings, or other formally published context

Thermal conductivity in self-assembled $CoFe_2O_4/BiFeO_3$ vertical nanocomposite films

Chen Zhang,[1,a)] Samuel C. Huberman,[2] Shuai Ning,[1] Jonathan Pelliciari,[3] Ryan A. Duncan,[3] Bolin Liao,[2] Shuchi Ojha,[1] John W. Freeland,[4] Keith A. Nelson,[5] Riccardo Comin,[3] Gang Chen,[2] and Caroline A. Ross[1,b)]

[1]*Department of Materials Science and Engineering, Massachusetts Institute of Technology, Cambridge, Massachusetts 02139, USA*
[2]*Department of Mechanical Engineering, Massachusetts Institute of Technology, Cambridge, Massachusetts 02139, USA*
[3]*Department of Physics, Massachusetts Institute of Technology, Cambridge, Massachusetts 02139, USA*
[4]*Advanced Photon Source, Argonne National Laboratory, Argonne, Illinois 60439, USA*
[5]*Department of Chemistry, Massachusetts Institute of Technology, Cambridge, Massachusetts 02139, USA*

(Received 19 July 2018; accepted 7 November 2018; published online 28 November 2018)

The thermal conductivity of self-assembled nanocomposite oxide films consisting of cobalt ferrite (CFO) spinel pillars grown within a single-crystal bismuth ferrite (BFO) perovskite matrix is described as a function of the volume fraction of the spinel. Single phase BFO and CFO had cross-plane thermal conductivities of 1.32 $W\,m^{-1}\,K^{-1}$ and 3.94 $W\,m^{-1}\,K^{-1}$, respectively, and the thermal conductivity of the nanocomposites increased with the CFO volume fraction within this range. A small increase (~5%) in thermal conductivity for the pure CFO phase in the AC-demagnetized state was observed, suggesting possible magnon contributions. Steady state gray-medium based variance-reduced Monte Carlo simulations show consistent trends with experimental data on the dependence of thermal conductivity with the CFO volume fraction. *Published by AIP Publishing.*
https://doi.org/10.1063/1.5049176

The importance of nanoscale heterogeneity in determining thermal transport in materials is well established.[1–3] The thermal transport properties of a heterogeneous system depend on the nature of the materials present, their volume fractions, the structure and geometry of the interfaces, and the length scale of the modulation with respect to the mean free path of the thermal carriers.[4–12] Thermal transport has been characterized and modeled in a wide variety of heterogeneous materials with planar interfaces parallel to the substrate[13–16] and in materials with randomly oriented interfaces such as nanocrystalline materials[17] or nanoparticles embedded in a matrix.[18] There has been less work on thin film systems with interfaces normal to the film plane. Heat conduction has been characterized in columnar polycrystalline diamond films[19–21] and metallic films[22] with vertical grain boundaries and in etched mesoscale structures with interfaces perpendicular to the substrate.[23] Self-assembled heteroepitaxial nanocomposite films, in which one phase grows as columns oriented out-of-plane within another phase and both phases are epitaxial with the substrate, provide a model system with well-defined vertical interfaces.[24–28] These structures allow the contribution of interfaces to thermal properties to be quantified. Notably, a ferroelectric or magnetostrictive strain at the interfaces can be induced and manipulated by applying an external electric or magnetic field, which leads to coupling phenomena including magnetoelectricity[24–26] and magneto-luminescence.[28] Understanding phonon transport in multiferroic nanocomposites will be useful for developing multifunctional thermoelectric devices and manipulating phonon transport via external fields.

In this work, we measure the thermal conductivity of spinel/perovskite nanocomposites consisting of pillars of ferrimagnetic $CoFe_2O_4$ (CFO) in a matrix of ferroelectric $BiFeO_3$ (BFO) grown on single crystal (001) $SrTiO_3$ (STO) substrates by pulsed laser deposition (PLD). We use time domain thermoreflectance (TDTR) to measure the thermal conductivity of nanocomposite films in the cross-plane direction normal to the substrate, i.e., parallel to the pillars, as a function of the volume fraction of CFO.

The spinel/perovskite films were grown by codeposition of CFO and BFO from two separate targets on STO (001) substrates at 750 °C using combinatorial pulsed laser deposition (PLD) with a 248 nm wavelength ArF laser as described previously.[29] The targets were ablated alternately and the substrate holder was rotated 180° every time the targets were exchanged. Each "layer" of material deposited from either target was less than one monolayer thick (~0.4 nm), ensuring that continuous in-plane multilayers did not form. Instead, diffusion of arriving species on the surface led to the growth of CFO pillars in a BFO matrix. The coordinated motion of the substrate holder and targets during growth led to a set of samples with a range of CFO:BFO ratios.

The area fraction, pillar size, and pillar interface length per unit area were obtained by image processing of top-down SEM micrographs. The CFO pillar areas were determined by ImageJ software and the total perimeter was calculated assuming that they each had a square cross-section, yielding the interface density. The volume fraction of CFO was taken as equal to the area fraction of pillars in the SEM images on the assumption that the pillars have vertical facets.[30] For each image, a threshold pillar area was set such that small pillars or features of order 5 nm diameter and below were excluded from the analysis.

a)Present address: School of Information Science and Engineering, Shandong University, Qingdao 266237, China
b)Author to whom correspondence should be addressed: caross@mit.edu

TABLE I. The parameters used as input in the fitting of a three-layer heat diffusion equation.

	Thermal conductivity (W/m K)	Volumetric heat capacity C, 300 K (J/m^3 K)	Layer thickness
Al	236.8	2.490×10^6	85 nm
CFO_xBFO_{1-x}	κ	$xC_{CFO} + (1-x)C_{BFO}$ ($C_{CFO} = 3.445 \times 10^6$, $C_{BFO} = 3.074 \times 10^6$)	50 nm
STO	11.2	2.617×10^6	500 μm

Magnetic hysteresis of the samples was measured using a vibrating sample magnetometer (ADE VSM) in fields up to 10 kOe. X-ray absorption spectroscopy (XAS) and x-ray magnetic circular dichroism (XMCD) were measured at the Advanced Photon Source at Argonne National Laboratory using beamline 4-ID-C. A magnetic field of 3.36 kOe was applied normal to the film plane and XAS was measured in total electron yield (TEY) and total fluorescence yield (TFY) modes. The cross-plane thermal conductivity was measured by TDTR[31–33] at 300 K and 220 K. Aluminum layers with a thickness of ~85 nm were deposited on the nanocomposite films to serve as a transducer. By measuring the time-dependent reflectivity of the metallic Al overlayer after heating with a pulsed pump laser (wavelength 400 nm, pulse width 200 fs, and spot size 50 μm) using a time-delayed probe laser (wavelength 800 nm, modulation frequencies 3, 6, 9, and 12 MHz, and spot size ~50 μm), the thermal transport properties in the underlying thin film were extracted by fitting to a three-layer heat diffusion equation for the cooling of the sample,[32] Table I. The layer structure consists of the Al film, the nanocomposite film, and a finite thermal interface conductance separating them.

SEM images of four nanocomposite samples are illustrated in Fig. 1. The thickness of each sample was 51 nm, as indicated by the X-ray reflectivity (XRR) measurement and

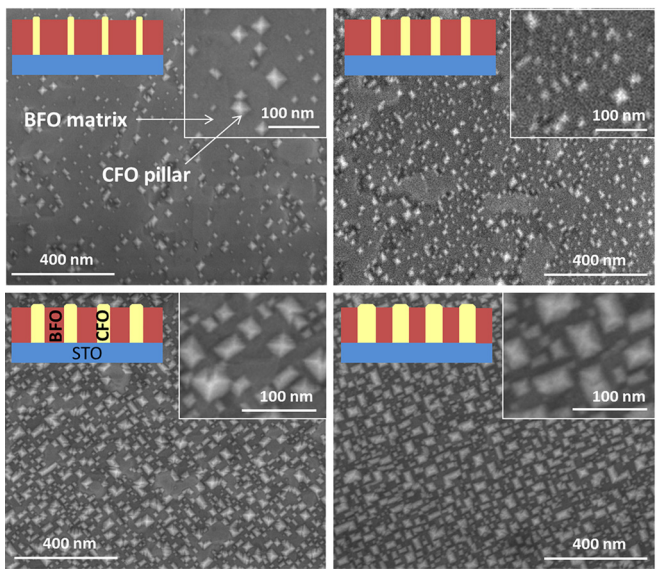

FIG. 1. SEM top view images of four BFO/CFO nanocomposites of increasing CFO volume fraction. The left insets show the structure schematically and the right insets show higher magnification images.

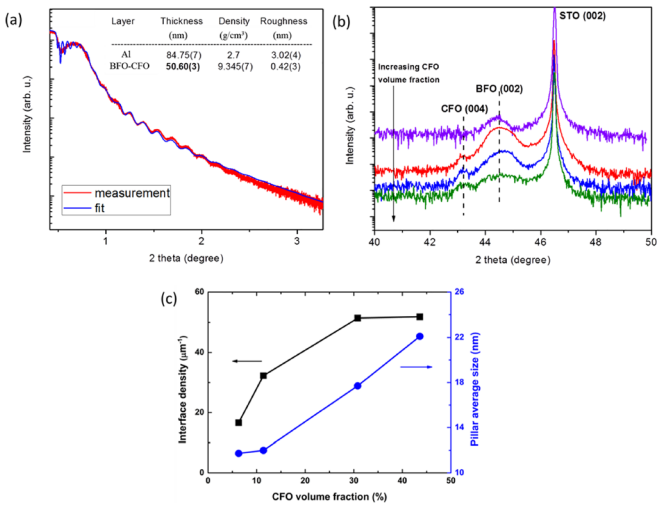

FIG. 2. (a) XRR thickness measurement and fitting of the nanocomposite film and Al overlayer. (b) $\omega-2\theta$ scans of the nanocomposites showing the CFO, BFO, and STO peaks. (c) Pillar size and interface density as a function of the volume fraction of CFO, based on SEM image analysis.

fitting, Fig. 2(a). The pillars protrude slightly at the surface, and the average surface roughness was ~0.42 nm. X-ray diffraction (XRD), Fig. 2(b), shows the presence of both spinel and perovskite peaks consistent with the phase-separated morphology, with the CFO peak intensity increasing with the volume fraction. Prior work has shown that the BFO grows with cube-on-cube epitaxy on the STO, i.e., $\langle 001 \rangle_{BFO}$ is parallel to $\langle 001 \rangle_{STO}$. The CFO is also cube-on-cube epitaxial with the STO (its lattice parameter is close to twice that of the BFO and STO) and grows as rectangular pillars with {110} vertical facets within the BFO matrix.[29]

Figure 2(c) shows the average pillar edge length and the interface density as a function of the volume fraction of CFO, which varied from 6.3% to 43.6%. The interface density initially increased with the increasing volume fraction but was almost the same for the two samples with the highest volume fraction. The average pillar edge length was similar for the two samples with the lowest volume fraction but then increased with the volume fraction. The trends suggest that for small CFO flux, there is an increasing probability of pillar nucleation with increasing flux, but above a certain volume fraction (here above ~12%), additional flux contributes to increasing the size of the pillars rather than nucleating new ones. There is considerable distribution of pillar sizes and spacings, but the average spacing is on the order of 50 nm and average pillar diameters are 12–22 nm.

The magnetic hysteresis loops of one of the samples are shown in Fig. 3(a). Other samples showed similar loop shapes. The magnetic hysteresis originates from the CFO pillars, and the BFO, a canted antiferromagnet, contributes negligibly. All the samples show similar saturation magnetization normalized by CFO volume fraction, of order 50–60 emu cm^{-3}. The magnetization is low compared to that of bulk CFO [~400 emu cm^{-3} (Ref. 34)] which is attributed to the non-ideal stoichiometry of the CFO pillars. Growth of single phase CFO films from the same target under similar PLD conditions led to excess Co such that Co:Fe ~1.4:2 instead of the stoichiometric ratio of 1:2. As shown in Fig. 3(b), increasing the Fe content of single-phase CFO by combinatorial deposition from CFO and Fe_3O_4 targets

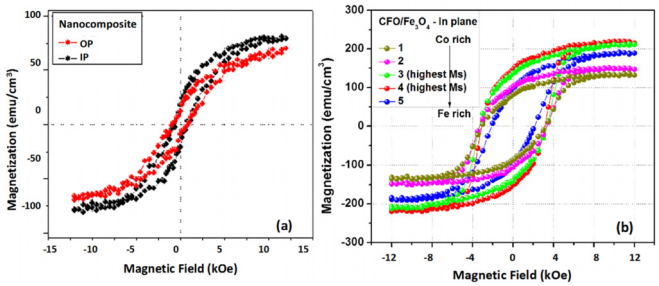

FIG. 3. (a) VSM hysteresis loops of the nanocomposite corresponding to the bottom left sample in Fig. 1, normalized to the CFO volume, measured with out-of-plane (OP) and in-plane (IP) field. (b) IP hysteresis loops of CFO grown with increasing amounts of codeposited Fe_3O_4. Sample 4 has the composition closest to stoichiometric CFO.

led to an increase in the magnetization of the film. However, the nanocomposites were not deposited with additional Fe_3O_4 and the pillars are therefore assumed to approximate the $Co_{1.2}Fe_{1.8}O_4$ composition obtained from the CFO target corresponding to sample 1 of Fig. 3(b).

Both Co^{2+} and Co^{3+} have a preference for the octahedral (O_h) sites in spinel, but the degree of inversion (site occupancy) of the spinel can depend on its preparation conditions.[35,36] The magnetic moments on the tetrahedral (T_d) and octahedral sites are coupled antiferromagnetically, so for stoichiometric $CoFe_2O_4$ without oxygen deficiency, which can be written as $[Fe^{3+}]_{tet}[Fe^{3+}, Co^{2+}]_{oct}O_4$, the net magnetic moment is due only to the Co^{2+} O_h because the Fe^{3+} moments cancel out. For the $Co_{1.2}Fe_{1.8}O_4$ spinel, which can be written as $[Fe^{3+}]_{tet}[Fe^{3+}{}_{0.8}\ Co^{3+}{}_{0.2}\ Co^{2+}{}_{1.0}]_{oct}O_4$, the Fe magnetic moments no longer compensate each other. The net magnetic moment is then expected to be lower than for $CoFe_2O_4$.

The XAS and XMCD results (Fig. 4) of two nanocomposites, which were grown at a different time from those of Fig. 1 but under similar conditions, show that both Co and

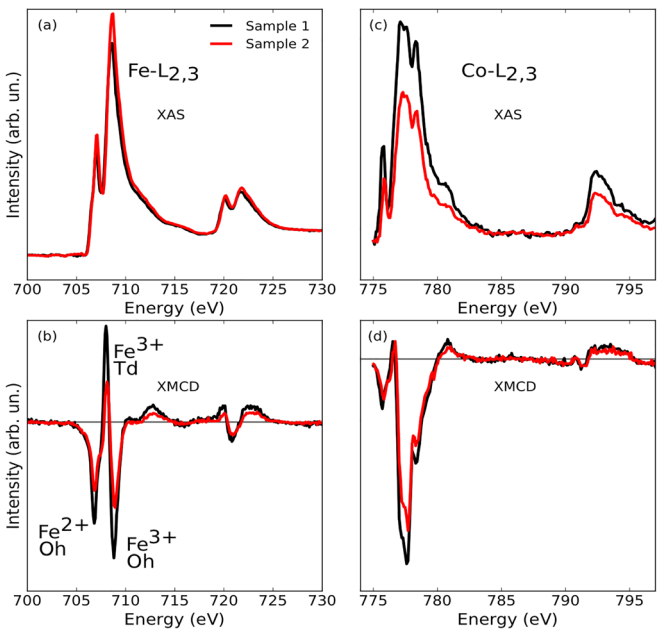

FIG. 4. (a) and (c) XAS and (b) and (d) XMCD of BFO-CFO nanocomposites measured in the TEY mode, for (a) and (b) Fe and (c) and (d) Co. Red and black data represent measurements from two different samples.

Fe have a non-zero net magnetic moment as displayed by the presence of dichroism in Figs. 4(b) and 4(d). By comparing the profile of the Fe XAS [Fig. 4(a)] with prior reports, we find that Fe is primarily in the Fe^{2+} and Fe^{3+} ionic states, and while we cannot rule out a contribution from Fe^{3+} in the BFO, which has a weak magnetism due to antiferromagnetic canting, the latter is too small to account for the Fe XMCD.[37–42] The XAS of cobalt reported in Fig. 4(c) indicates a mixed oxidation state comprising mainly Co^{2+} and Co^{3+}. This observation is consistent with an imbalance between Fe site from the O_h and T_d sublattices, as expected from the excess Co present at the octahedral sites. Indeed, the XMCD lineshape in Fig. 4(b) reveals the presence of Fe^{2+} and Fe^{3+} O_h and Fe^{3+} T_d.[37–40] The XMCD signal observed on the Co site indicates that the direction of the spins is parallel to Fe^{2+}/Fe^{3+} O_h and opposite to the Fe^{3+} T_d, which further corroborates the hypothesis of an inverse spinel. The same XAS and XMCD results have been observed in total fluorescence yield corresponding to the bulk (Fig. S1 in the Supplementary Material).

The magnetization and other properties such as magnetocrystalline anisotropy and magnetostriction are sensitive to the chemical distribution and valence states of the cations on the octahedral and tetrahedral sites. Cation off-stoichiometry in CFO is known to lower the magnetization, both for Co-rich[34] and Co-deficient[43] compositions, and can lead to formation of secondary phases such as (antiferromagnetic) rocksalt structures. Excess Co also dramatically reduces the magnetostriction in bulk CFO.[34] In the nanocomposite, there also exists the possibility of cation exchange with the BFO, although prior work did not show significant Co incorporation into BFO.[30]

The loops for the nanocomposites for out-of-plane field and in-plane field are similar indicating less magnetic anisotropy than for previously reported nanocomposites.[29,30] The anisotropy originates from magnetoelastic anisotropy due to the out-of-plane compressive strain state of the CFO caused by its lattice mismatch with the BFO at the vertical interfaces and shape anisotropy from the pillars. Magnetocrystalline anisotropy does not contribute to the difference between the in-plane (field in the [100] direction) and out-of-plane (field in the [001] direction) loops. The low anisotropy of the samples is attributed to two factors. First, the lower magnetostriction of the off-stoichiometric CFO reduces the contribution of magnetoelastic anisotropy. Second, the low film thickness limits the pillar aspect ratio (height/diameter) which in combination with the low magnetic moment reduces the shape anisotropy.

Figure 5(a) shows the thermal conductivity extracted from TDTR of the nanocomposites plotted vs. CFO volume fraction. We reported a thermal conductivity of $1.32\,W\,m^{-1}\,K^{-1}$ for single-phase BFO films,[44] and we measured a thermal conductivity of $3.7–3.9\,W\,m^{-1}\,K^{-1}$ for single-phase CFO films grown on (110) STO with Co:Fe = 1:2, Fig. 5(b). An interesting result for the single-phase CFO is that the thermal conductivity had a small dependence on the magnetization state, with the conductivity of DC-magnetized films (i.e., at remanence after saturation) approximately 5% smaller than that of AC-demagnetized films, Fig. 5(b). The insets show magnetic force microscopy images, with the contrast indicating magnetic

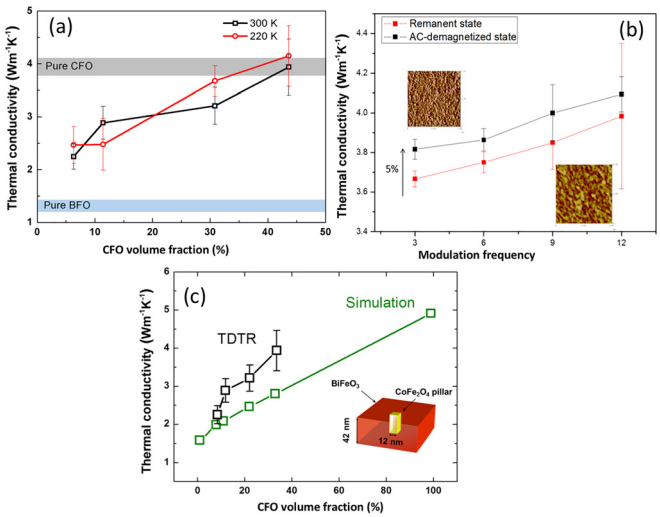

FIG. 5. (a) Dependence of cross-plane thermal conductivity on the CFO volume fraction at 220 K and 300 K measurement temperature; (b) thermal conductivity of a CFO single phase film grown on STO (110) measured at different modulation frequencies, both in a dc-remanent state and after ac-demagnetization. The insets are 2 μm × 2 μm magnetic field microscopy images of the sample showing finer, higher contrast domain patterns in the ac-demagnetized state (color scale: 2° phase); (c) simulated cross-plane thermal conductivity versus CFO volume fraction. Inset: Schematics of the simplified geometry used in the steady state gray variance-reduced Monte Carlo simulation.

domains. The domain-wall-dependent thermal conductivity shares some analogies with the case of ferroelectric materials, in which Hopkins *et al*. demonstrated the effect of the ferroelectric domain structure on thermal conductivity.[45,46] However, the CFO shows an *increased* thermal conductivity with an increased number of vertical magnetic domain walls, suggesting possible contributions from magnons.

The dependence of thermal conductivity on modulation frequency is weak and largely within the error bar. The causes for this dependence are not clear at this stage but it may represent a systematic error due to changes in sensitivity to the thin film thermal conductivity as a function of frequency. At low frequencies, the measurement is sensitive to the substrate and the nanocomposite film, while at high frequencies, it is sensitive to the interface between the aluminum and the nanocomposite film, which has a higher conductance. The results are insensitive to the thermal conductivity of the Al so long as it is greater than 150 W/mK which is expected in even poor quality Al films.[47]

For the nanocomposites, the thermal conductivity scales approximately linearly with the CFO volume fraction, increasing by a factor of ~2 in the range of 6.3–43.6 vol. % CFO. The interface density appears to be less significant, since the two highest volume fraction samples have similar interface densities but different thermal conductivities. The thermal conductivity at 220 K is slightly higher or similar to that measured at 300 K. An increase in thermal conductivity with decreasing temperature is expected in single crystals due to the reduction in phonon-phonon scattering and increase in the mean free path of the phonons at low temperature. Boundary scattering, if important, tends to reduce this temperature dependence, which limits the enhancement in thermal conductivity as the temperature decreases. The thermal conductivity of the composite at 45% CFO concentration is comparable to that of the single-phase CFO. This could be caused by two factors: the composite contains $Co_{1.2}Fe_{1.8}O_4$, whereas the single phase sample is $CoFe_2O_4$, and the strain states of CFO are different in the composites and single phase CFO.[48]

The thermal conductivity plotted versus volume fraction is roughly linear [Fig. 5(c)], although at a low volume fraction, the thermal conductivity drops below the linear trend. This is mainly an effect of the size of the CFO pillars since at a low volume fraction, the diameter of the pillars is smaller [Fig. 2(c)]. These behaviors are expected via classical size effects due to diffuse boundary phonon scattering at interfaces.

Since first-principles calculations of thermal conductivity of such complex unit cells is difficult, we use a constant phonon mean free path as input to Monte Carlo (MC) simulation to show trends. The simulation employs the variance-reduced Monte Carlo (MC) method[49,50] and was carried out at room temperature. MC simulations have been applied to study the phonon transport and scattering mechanism in Si nanowires,[51,52] nitride,[53] and graphene nanoribbons.[54] The variance-reduced MC simulation accelerates the simulation significantly, enabling treating complicated geometries. For the MC model, the hot side temperature was fixed at 301 K and the cold side temperature was fixed at 300 K. The film thickness was 42 nm. Two sets of gray properties were manipulated to achieve the pure values of BFO and CFO. The model consisted of a matrix and a single centered pillar, where the square pillar had sides of length 12 nm. The remaining matrix dimensions were set to maintain the desired volume fraction. The probability of transmission between the pillar and the matrix was fixed at 0.5, and boundaries are assumed to be diffuse. The linear increase in thermal conductivity with the CFO volume fraction is reproduced by simulation [Fig. 5(c)], including the steeper rise at small volume fractions.

Transient thermal grating (TTG) spectroscopy was used to characterize the in-plane thermal conductivity perpendicular to the pillar axis. Two interfering laser beams produce a spatially modulated thermal profile in an absorbing layer whose decay is measured by the diffraction of a probe beam.[55,56] However, based on modeling of the effect of the film thickness and on the bulk thermal conductivities of STO and BFO, the analysis was insensitive to variations in the film in-plane thermal conductivity due to the dominant effect of the substrate. This precluded identification of a trend in the in-plane thermal conductivity of the samples.

In summary, self-assembled BFO/CFO vertical nanocomposite films with volume fractions of CFO in the range of 6.3%–43.6% were grown via combinatorial pulsed laser deposition. The cross-plane thermal conductivity, in which the heat flow is parallel to the BFO/CFO interfaces, increased approximately linearly with the CFO content from 2.25 $W\,m^{-1}\,K^{-1}$ to 3.94 $W\,m^{-1}\,K^{-1}$ at room temperature, between the thermal conductivities of single-phase BFO and CFO. A small increase (~5%) in thermal conductivity for the pure CFO phase in the AC-demagnetized state was observed. Steady state gray-medium based variance-reduced Monte Carlo simulations at room temperature show a trend

in the thermal conductivity dependence on the CFO volume fraction consistent with experimental data.

See supplementary material for additional XMCD data acquired using the total fluorescence yield mode.

This work was supported as part of the Solid-State Solar-Thermal Energy Conversion Center (S3TEC), an Energy Frontier Research Center funded by the U.S. Department of Energy, Office of Science, Basic Energy Sciences under Award No. # DE-SC0001299. This work made use of shared experimental facilities of CMSE, supported under NSF DMR1419807. J.P. acknowledges financial support by the Swiss National Science Foundation Early Postdoc. Mobility fellowship Project No. P2FRP2_171824 and Postdoc. Mobility Project No. P400P2_180744. Work at the Advanced Photon Source, Argonne, was supported by the U.S. Department of Energy, Office of Science under Grant No. DEAC02-06CH11357. The authors greatly appreciate technical advice from Dr. Alexei Maznev of MIT.

[1]D. G. Cahill, W. K. Ford, K. E. Goodson, G. D. Mahan, A. Majumdar, H. J. Maris, R. Merlin, and S. R. Phillpot, J. Appl. Phys. **93**(2), 793–818 (2003).
[2]E. T. Swartz and R. O. Pohl, Rev. Mod. Phys. **61**, 605–668 (1989).
[3]A. Giri, J. L. Braun, and P. E. Hopkins, J. Appl. Phys. **119**, 235305 (2016).
[4]G. Chen, J. Heat Transfer **119**, 220–229 (1997).
[5]V. Narayanamurti, H. L. Stormer, M. A. Chin, A. C. Gossard, and W. Wiegmann, Phys. Rev. Lett. **43**, 2012–2016 (1979).
[6]G. Chen, Phys. Rev. B **57**, 14958 (1998).
[7]R. M. Costescu, M. A. Wall, and D. G. Cahill, Phys. Rev. B **67**, 054302 (2003).
[8]M. V. Simkin and G. D. Mahan, Phys. Rev. Lett. **84**, 927 (2000).
[9]Y. K. Koh, Y. Cao, D. G. Cahill, and D. Jena, Adv. Funct. Mater. **19**, 610–615 (2009).
[10]M. N. Luckyanova, J. Garg, K. Esfarjani, A. Jandl, M. T. Bulsara, A. J. Schmidt, A. J. Minnich, S. Chen, M. S. Dresselhaus, Z. Ren, E. A. Fitzgerald, and G. Chen, Science **338**, 936–939 (2012).
[11]A. K. Roy, B. L. Farmer, V. Varshney, S. Sihn, J. Lee, and S. Ganguli, ACS Appl. Mater. Interfaces **4**, 545–563 (2012).
[12]J. Ravichandran, A. K. Yadav, R. Cheaito, P. B. Rossen, A. Soukiassian, S. J. Suresha, J. C. Duda, B. M. Foley, C.-H. Lee, Y. Zhu, A. W. Lichtenberger, J. E. Moore, D. A. Muller, D. G. Schlom, P. E. Hopkins, A. Majumdar, R. Ramesh, and M. A. Zurbuchen, Nat. Mater. **13**, 168 (2014).
[13]X. Wang and B. Huang, Sci. Rep. **4**, 6399 (2014).
[14]K. Kothari and M. Maldovan, Sci. Rep. **7**, 5625 (2017).
[15]M. Hijazi and M. Kazan, AIP Adv. **6**, 065024 (2016).
[16]B. Qiu, G. Chen, and Z. Tian, Nanoscale Microscale Thermophys. Eng. **19**, 272 (2015).
[17]S. K. Bux, R. G. Blair, P. K. Gogna, H. Lee, G. Chen, M. S. Dresselhaus, R. B. Kaner, and J.-P. Fleurial, Adv. Funct. Mater. **19**, 2445–2452 (2009).
[18]K. Biswas, J. He, Q. Zhang, G. Wang, C. Uher, V. P. Dravid, and M. G. Kanatzidis, Nat. Chem. **3**, 160–166 (2011).
[19]A. Sood, J. Cho, K. D. Hobart, T. I. Feygelson, B. B. Pate, M. Asheghi, D. G. Cahill, and K. E. Goodson, J. Appl. Phys. **119**, 175103 (2016).
[20]E. Bozorg-Grayeli, A. Sood, M. Asheghi, V. Gambin, R. Sandhu, T. I. Feygelson, B. B. Pate, K. Hobart, and K. E. Goodson, Appl. Phys. Lett. **102**, 111907 (2013).
[21]M. N. Touzelbaev and K. E. Goodson, Diamond Relat. Mater. **7**, 1–14 (1998).
[22]H. Ho, A. A. Sharma, W.-L. Ong, J. A. Malen, J. A. Bain, and J.-G. Zhu, Appl. Phys. Lett. **103**(13), 131907 (2013).
[23]K. Termentzidis, J. Parasuraman, C. A. Da Cruz, S. Merabia, D. Angelescu, F. Marty, T. Bourouina, X. Kleber, P. Chantrenne, and P. Basset, Nanoscale Res. Lett. **6**, 288 (2011).
[24]H. Zheng, J. Wang, S. Lofland, Z. Ma, L. Mohaddes-Ardabili, T. Zhao, L. Salamanca-Riba, S. Shinde, S. Ogale, and F. Bai, Science **303**, 661–663 (2004).
[25]A. Chen, Z. Bi, Q. Jia, J. L. MacManus-Driscoll, and H. Wang, Acta Mater. **61**, 2783–2792 (2013).
[26]W. Zhang, A. Chen, Z. Bi, Q. Jia, J. L. MacManus-Driscoll, and H. Wang, Curr. Opin. Solid State Mater. Sci. **18**, 6–18 (2014).
[27]L. Mohaddes-Ardabili, H. Zheng, S. B. Ogale, B. Hannoyer, W. Tian, J. Wang, S. E. Lofland, S. R. Shinde, T. Zhao, Y. Jia, L. Salamanca-Riba, D. G. Schlom, M. Wuttig, and R. Ramesh, Nat. Mater. **3**, 533–538 (2004).
[28]C. Zhang, D. H. Kim, X. Huang, X. Y. Sun, N. M. Aimon, S. J. Chua, and C. A. Ross, ACS Appl. Mater. Interfaces **9**(37), 32359–32368 (2017).
[29]N. M. Aimon, D. Hun Kim, H. Kyoon Choi, and C. A. Ross, Appl. Phys. Lett. **100**, 092901 (2012).
[30]N. M. Aimon, H. K. Choi, X. Y. Sun, D. H. Kim, and C. A. Ross, Adv. Mater. **26**, 3063–3067 (2014).
[31]W. S. Capinski and H. J. Maris, Rev. Sci. Instrum. **67**, 2720–2726 (1996).
[32]D. G. Cahill, K. Goodson, and A. Majumdar, J. Heat Transfer **124**, 223–241 (2002).
[33]A. J. Schmidt, X. Chen, and G. Chen, Rev. Sci. Instrum. **79**, 114902 (2008).
[34]I. C. Nlebedim, A. J. Moses, and D. C. Jiles, J. Magn. Magn. Mater. **343**, 49–54 (2013).
[35]A. S. Vaingankar, B. V. Khasbardar, and R. N. Patil, J. Phys. F: Met. Phys. **10**, 1615–1619 (1980).
[36]G. A. Sawatzky, F. Van Der Woude, and A. H. Morrish, Phys. Rev. **187**, 747 (1969).
[37]Y. K. Wakabayashi, Y. Nonaka, Y. Takeda, S. Sakamoto, K. Ikeda, Z. Chi, G. Shibata, A. Tanaka, Y. Saitoh, H. Yamagami, M. Tanaka, A. Fujimori, and R. Nakane, Phys. Rev. B **96**, 104410 (2017).
[38]E. Pellegrin, M. Hagelstein, S. Doyle, H. O. Moser, J. Fuchs, D. Vollath, S. Schuppler, M. A. James, S. S. Saxena, L. Niesen, O. Rogojanu, G. A. Sawatzky, C. Ferrero, M. Borowski, O. Tjernberg, and N. B. Brookes, Phys. Status Solidi B **215**, 797 (1999).
[39]R. A. D. Pattrick, G. van der Laan, C. M. B. Henderson, P. Kuiper, E. Dudzik, and D. J. Vaughan, Eur. J. Mineral. **14**, 1095–1102(8) (2002).
[40]C. I. Pearce, C. M. B. Henderson, R. A. D. Pattrick, G. van der Laan, and D. J. Vaughan, Am. Mineral. **91**, 880 (2006).
[41]E. Arenholz, G. van der Laan, R. V. Chopdekar, and Y. Suzuki, Phys. Rev. B **74**, 094407 (2006).
[42]J. S. Bettinger, C. Piamonteze, R. V. Chopdekar, M. Liberati, E. Arenholz, and Y. Suzuki, Phys. Rev. B **80**, 140413(R) (2009).
[43]I. C. Nlebedim, J. E. Snyder, A. J. Moses, and D. C. Jiles, J. Appl. Phys. **111**, 07D704 (2012).
[44]S. Ning, S. C. Huberman, C. Zhang, Z. Zhang, G. Chen, and C. A. Ross, Phys. Rev. Appl. **8**, 054049 (2017).
[45]J. F. Ihlefeld, B. M. Foley, D. A. Scrymgeour, J. R. Michael, B. B. McKenzie, D. L. Medlin, M. Wallace, S. Trolier-McKinstry, and P. E. Hopkins, Nano Lett. **15**, 1791 (2015).
[46]B. M. Foley, M. Wallace, J. T. Gaskins, E. A. Paisley, R. L. Johnson-Wilke, J.-W. Kim, P. J. Ryan, S. Trolier-McKinstry, P. E. Hopkins, and J. F. Ihlefeld, ACS Appl. Mater. Interfaces **10**, 25493 (2018).
[47]A. Schmidt "Optical characterization of thermal transport from the nano-scale to the macroscale," Ph.D. thesis (Department of Mechanical Engineering, Massachusetts Institute of Technology, 2008).
[48]X. Li, K. Maute, M. L. Dunn, and R. Yang, Phys. Rev. B **81**, 245318 (2010).
[49]J.-P. M. Peraud and N. G. Hadjiconstantinou, Phys. Rev. B **84**, 205331 (2011).
[50]J.-P. M. Peraud and N. G. Hadjiconstantinou, Appl. Phys. Lett. **101**, 153144 (2012).
[51]Y. Chen, D. Li, J. R. Lukes, and A. Majumdar, J. Heat Transfer **127**, 1129 (2005).
[52]V. Jeana, S. Fumerona, K. Termentzidisa, X. Ziannibc, and D. Lacroix, Int. J. Heat Mass Transfer **86**, 648 (2015).
[53]M. Farahmand, C. Garetto, E. Bellotti, K. F. Brennan, M. Goano, E. Ghillino, G. Ghione, J. D. Albrecht, and P. Paul Ruden, IEEE Trans. Electron Devices **48**, 535 (2001).
[54]S. Mei, L. N. Maurer, Z. Aksamija, and I. Knezevic, J. Appl. Phys. **116**, 164307 (2014).
[55]J. A. Rogers, A. A. Maznev, M. J. Banet, and K. A. Nelson, Annu. Rev. Mater. Sci. **30**, 117 (2000).
[56]O. W. Käding, H. Skurk, A. A. Maznev, and E. Matthias, Appl. Phys. A **61**, 253 (1995).